Vortex Flow Interaction Phenomena on Multi Swept Delta Wings at Subsonic Speeds

S. Pfnür[1], A. Hövelmann[2], D. Sedlacek[1], C. Breitsamter[1]

[1]Technical University of Munich, Department of Mechanical Engineering, Chair of Aerodynamics and Fluid Mechanics, Boltzmannstr. 15, 85748 Garching
GERMANY

[2]Airbus Defence and Space GmbH
Rechliner Str.
85077 Manching
GERMANY

stefan.pfnuer@tum.de

ABSTRACT

Experimental investigations on a low-aspect-ratio multiple-swept wing fuselage configuration are presented. The investigated configuration and test cases are embedded in the NATO STO AVT-316 task group on "Vortex Interaction Effects Relevant to Military Air Vehicle Performance". Two different wing planforms of the configuration are discussed. The so-called NA1 W1 and NA1 W2 configurations are equipped with triple and double delta wing planforms, respectively. Force and moment measurements as well as flowfield measurements were performed at low subsonic speeds. The analysis comprises the discussion of the flowfield and the wall-near flow dominated by a system of two interacting leading-edge vortices consisting of an inboard vortex and a midboard vortex. Furthermore, the flight physical stability and performance parameters are discussed and the characteristics are related to the flowfield phenomena. The results highlight the different stages of vortex interaction with respect to the angle of attack and the effect of vortex bursting on the vortex interaction. The inboard vortices develop at non-slender or slender wing sections for the NA1 W1 or NA1 W2 configurations, respectively. The inboard wing section, thus, dominates the bursting characteristics of the inboard vortices, which are of different abruptness and at different angles of attack. The magnitude of the flight mechanics instabilities are smaller and the instability onsets are smoother for the NA1 W1 configuration than for the NA1 W2 configuration. This is predominantly associated with the smoother vortex bursting characteristics of the inboard vortex at the NA1 W1 configuration.

NOMENCLATURE

C_D, C_Y, C_L	Drag, side force and lift coefficient, [-]
C_{mx}, C_{my}, C_{mz}	Rolling, pitching and yawing moment coefficient, [-]
$C_{mx\beta}$	Lateral stability parameter, [1/rad]
$C_{mz\beta}$	Directional stability parameter, [1/rad]
$C_{mz\beta,dyn}$	Dynamic directional stability parameter, [1/rad]
c_r	Root chord, [m]
d	Seeding particle diameter, spatial resolution, [m]
f_{meas}	Sampling frequency, [Hz]
I_X, I_Z	Moment of inertia about the x and z axis, [kg/m^2]
l_i	Length of wing section i, [m]

l_{Re}	Reynolds length, [m]
l_{tot}	Total length, [m]
l_μ	Mean aerodynamic chord, [m]
Ma	Mach number, [-]
Re	Reynolds number, [-]
S_{ref}	Wing reference area, [m^2]
s	Wing half span, [m]
T	Temperature, [K]
t_{meas}	Measurement time, [s]
U_∞	Freestream velocity, [m/s]
u,v,w	Velocity along the x, y and z axis, [m/s]
x,y,z	Body-fixed coordinates, [m]
x_{mrp}	x-coordinate of moment reference point, [m]
α	Angle of attack, [deg]
β	Angle of sideslip, [deg]
λ	Wing taper ratio, [-]
φ	Leading-edge sweep, [deg]
ω_x	Axial vorticity, [1/s]

1.0   INTRODUCTION

High-agile aircraft configurations typically feature wings of low aspect ratio and medium to high leading-edge sweep. Such wings exhibit a vortex dominated flowfield. The leading-edge vortices enable the exploitation of favourable non-linear lift characteristics. There have been extensive investigations on the characteristics of leading-edge vortices, which develop at slender and non-slender wings, cf. [1,2,3,4]. The leading-edge vortices are already observable at low angles of attack. As the angle of attack increases, the leading-edge vortices become unstable and start to burst in consequence of an arising adverse pressure gradient towards the wing trailing edge. Wings with a high leading-edge sweep of $\varphi > 60\,\mathrm{deg}$ are subject to a vortex breakdown associated with an abrupt and significant divergence of the vortex cross section, a reverse core flow and strong velocity fluctuations in the vortex core, cf. [1,2,3]. The position of the flow reversal in the vortex core is defined as the breakdown location for this type of leading-edge vortex.

As the leading-edge sweep decreases, the vortex breakdown is observed at lower angles of attack. At non-slender and semi-slender wings with a leading-edge sweep of $50\,\mathrm{deg} < \varphi < 60\,\mathrm{deg}$ there is also a change in the vortex breakdown characteristics, see [4]. The vortex breakdown is less abrupt and begins with the transition from a jet-type to a wake-type axial core flow over a certain region. The flow reversal of the axial core flow does not necessarily occur. Compared to the vortex breakdown at slender wings, the expansion of the vortex core is less abrupt. This makes it more difficult to clearly define the vortex breakdown location [4].

Wentz and Kohlman investigated the vortex breakdown at flat plate delta wings with leading-edge sweep angles of $45\,\mathrm{deg} \leq \varphi \leq 85\,\mathrm{deg}$ [5]. According to them, the vortex breakdown takes place at lower angles of attack for lower leading-edge sweeps. For sideslip conditions, the vortex breakdown becomes asymmetric.

The effective leading-edge sweep decreases at the windward side and increases at the leeward side. This results in a more upstream vortex bursting onset at the windward side, see Ref. [6]. The effect of asymmetric vortex breakdown on the surface pressure distribution of delta wings was investigated by Verhaagen and Jobe [7]. Johnson et al. [8] investigated the adverse effect of asymmetric vortex breakdown on the lateral-directional stability of highly-swept wings. Longitudinal, lateral and directional flight mechanics instabilities like a pitch-up, roll-reversal, and directional divergence result from the leading-edge vortex breakdown characteristics. These instabilities were observed for generic low-aspect ratio wing-body configurations [6] and for several types of high-performance aircraft, cf. Refs. [9,10,11,12].

Different measures can be found in the literature aiming at alleviating or eliminating the occurring instabilities for high-agile aircraft configurations. Geometric variations of details of such configurations have been investigated. These include the position and size of the vertical tails, see Refs. [10,13], the application of leading-edge/vortex flaps [10], the modification of the strake [14], or (fore)body geometry variations [15] and modifications, cf. Refs. [6,16,17,18]. All measures aim at the stabilization of the leading-edge vortex and consequently the shift of the vortex breakdown to higher angles of attack.

Another approach to tackle the instabilities is the intended triggering of the development of multiple, interacting leading-edge vortices. The development of multiple leading-edge vortices is determined by the corresponding wing planform. The spatial proximity of the leading-edge vortices results in their interaction, which has an influence on the vortex characteristics and consequently, on the global aerodynamic characteristics. The interaction is intended to be provoked in a way that entails a stabilizing effect on the vortex system and thus, improves the global flight mechanics stability and control. The flow physics of the interacting leading-edge vortices need to be well known to be able to evaluate the potential of the approach. Force and moment, surface, and flowfield measurements give a comprehensive database to analyse the flow physics of the interacting vortex system and its effect on the flight mechanical stability. In the study at hand, a low aspect ratio wing fuselage configuration with multiple swept wings is investigated at symmetric and asymmetric freestream conditions.

2.0   EXPERIMENTAL TECHNIQUE

2.1   Wind Tunnel Model, Test Facility, and Test Conditions

The investigated geometry is a generic low-aspect-ratio wing-fuselage configuration. The investigated model is subject to a common research program in cooperation with Airbus Defence and Space (Airbus DS) and the German Aerospace Center (DLR). Furthermore, it is embedded in the NATO AVT-316 task group called "Vortex Interaction Effects Relevant to Military Air Vehicle Performance". The wing of the configuration is designed as a flat plate with sharp leading edges. The model can be equipped with wings of different planform. The so-called NA1 W1 configuration is a triple delta wing configuration with three different consecutive wing sections featuring a varying leading-edge sweep, see Figs. 20-1 a) and b). The so-called NA1 W2 configuration is a double delta wing configuration with two different consecutive wing sections of varying leading-edge sweeps, see Figs. 20-1 c) and d). Detailed information on the geometric parameters of both configurations is summarized in Tab. 1. Due to the sharp wing leading edges, trip dots were only attached to the fuselage nose to force turbulent boundary-layer characteristics. This ensures the comparability of the experimental data to numerical results obtained by (unsteady) Reynolds-averaged Navier-Stokes simulations associated with fully-turbulent boundary layers. The wind tunnel model was attached via a rear sting to a three-axis support, which allows for the adjustment of the angles of attack and sideslip, see Figs. 20-1 b) and d). Considering the flowfield measurements, parts of the wind tunnel model were painted black to reduce the laser light reflections observed by the cameras.

The experiments were carried out in two different wind tunnel (W/T) facilities of the the Chair of Aerodynamics and Fluid Mechanics of the Technical University of Munich (TUM-AER). The oil flow

measurements were performed in the W/T B. The W/T B is of Göttingen type with an open test section of $1.2 \times 1.55 \times 2.8 m^3$ (height x width x length). The maximum freestream velocity reads $U_{\infty,max} = 65 m/s$. The maximum turbulence intensity is 0.4%, the uncertainty in the freestream direction is below 0.5 deg, the maximum uncertainty in the temporal and spatial mean velocity distribution is 0.67%, and the maximum static pressure variation along the test section is 0.5 %.[1]
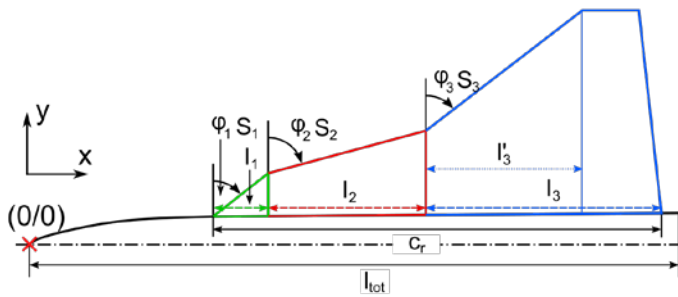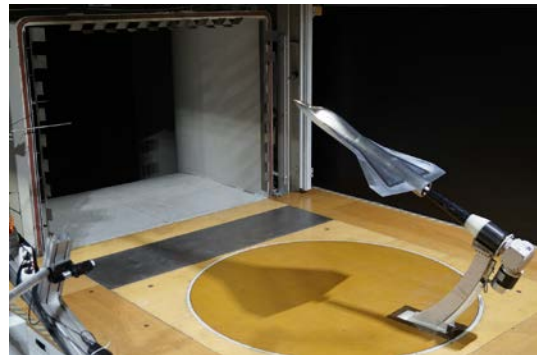

a) Planform sketch NA1 W1

b) NA1 W1 W/T model in the test section
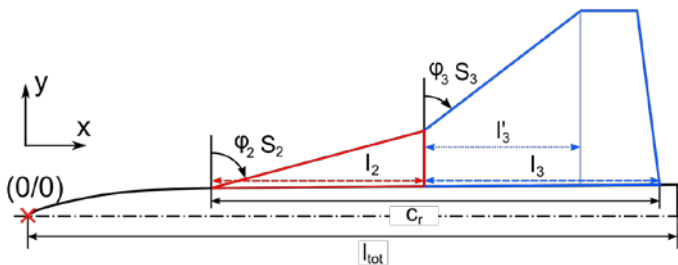
c) Planform sketch NA1 W2

d) NA1 W2 W/T model in test section

Figure 20-1: Wing planforms and wind tunnel model.

The force and moment as well as the flowfield measurements were conducted in the W/T A of the TUM-AER. The W/T was operated with an open test section which has a size of $1.8 \times 2.4 \times 4.8 m^3$ (height x width x length). In this condition, the maximum freestream velocity is $U_{\infty,max} = 65 m/s$ with a maximum turbulence intensity of 0.4% and an uncertainty in the freestream direction below 0.2 deg. The maximum uncertainty in the temporal and spatial mean velocity distribution is 0.67% and the static pressure variations along the test section is below 0.4%.[2]

The experiments in both test facilities were performed at low subsonic speeds with a Reynolds number of $Re = 3 \cdot 10^6$ based on the reference length $l_{Re} = 1m$ and a Mach number of $Ma = 0.15$. The force and moment measurements were performed for an angle of attack range of $0 \deg \le \alpha \le 40 \deg$ with an

---

[1] Data available online at https://www.aer.mw.tum.de/windkanaele/windkanal-b/ [retrieved 04 July 2019]

[2] Data available online at https://www.aer.mw.tum.de/windkanaele/windkanal-a/ [retrieved 04 July 2019]

increment of $\Delta\alpha = 1\deg$ at $\beta = 0\deg$ and $\beta = 5\deg$. The flowfield measurements are performed for the angles of attack $\alpha = \{8\deg, 16\deg, 24\deg, 32\deg\}$ at $\beta = 0\deg$ and for $\alpha = \{16\deg, 24\deg, 32\deg\}$ at $\beta = 5\deg$. The oil flow measurements were performed for $\alpha = 16\deg$ at $\beta = 0\deg$.

Table 20-1: Geometrical parameters of the NA1 W1 and NA1 W2 configurations

		NA1 W1	NA1 W2
c_r	[m]	0.802	0.802
s	[m]	0.417	0.367
S_{ref}	[m²]	0.329	0.266
AR	[-]	2.11	2.03
λ	[-]	0.15	0.16
l_{tot}	[m]	1.16	1.16
x_{mrp}	[m]	0.759	0.759
l_μ	[m]	0.468	0.426
l_1 / c_r	[-]	0.125	-
l_2 / c_r	[-]	0.35	0.475
l'_3 / c_r	[-]	0.35	0.35
l_3 / c_r	[-]	0.475	0.475
φ_1	[deg]	52.5	-
φ_2	[deg]	75	75
φ_3	[deg]	52.5	52.5
I_Z / I_X	[-]	3.93	3.93

2.3 Force and Moment Measurements

An internal six-component strain-gauge balance was used to acquire the aerodynamic forces and moments. The maximum sustainable loads read 900 N, 450 N, 2500 N for axial, lateral, and normal forces, respectively. The maximum sustainable moments are 120 Nm, 160 Nm, 120 Nm for rolling, pitching, and yawing moments, respectively. The temperature calibration of the balance comprises a temperature range of $283K \leq T \leq 328K$. The observed temperatures during the measurements were in a range of $291K \leq T \leq 308K$ and therefore within the calibrated temperature range. The forces and moments were measured with a sampling frequency of $f_{meas} = 800Hz$ for a total acquisition time of $t_{meas} = 10s$. The repeatability of the aerodynamic coefficients for the applied test setup reads $\Delta C_D \mp 0.0035$, $\Delta C_Y = \mp 0.0012$, $\Delta C_L = \mp 0.0051$, $\Delta C_{mx} = \mp 0.0005$, $\Delta C_{my} = \mp 0.0017$, and $\Delta C_{mz} = \mp 0.00042$. The repeatability is defined as the standard deviation of the coefficients determined from several angle-of-attack polar measurements. The standard deviation was determined for every angle of attack and coefficient. The mean of the standard deviations of the angle-of-attack polar corresponds to the presented repeatability.

2.4 Stereo Particle Image Velocimetry

A Stereo-PIV measurement system was used to measure the flowfield above the wing in several cross-flow sections. The Stereo-PIV system was mounted on a three-axis traversing system next to the W/T test section, see Fig. 20-2 a). The traversing system itself can be rotated around its vertical axis. Furthermore, the cameras and the laser sheet can be rotated around the traversing system's lateral axis. These two adjustments enable the alignment of the cameras and the laser sheet with the angle of attack and the angle of sideslip of the W/T model. A double pulsed Nd:Yag laser with a maximum power of 325 mJ per pulse and a wave length of 532nm illuminated the measurement plane. Two sCMOS cameras with a resolution of 2560×2160 pixel were placed up- and downstream of the measurement plane. The cameras were equipped with NIKON lenses with a focal length of 135mm. The sCMOS sensor planes were tilted by Scheimpflugadapters to meet the Scheimpflug criterion, cf. Ref. [19]. Seeding particles with a diameter of $d \approx 1 \mu m$ were fed into the flow.

The cameras recorded 400 image pairs per cross-flow section with a sampling frequency of $f_{meas} = 15 Hz$.

The presented quantities in this study are the mean values determined from the 400 acquired samples. The flowfield data of all the presented freestream conditions were acquired within two separate wind tunnel entries. This leads to differences in the setup, the post-processing parameters, and the resolution of the final field of view. The information on the setup for the first and second stereo-PIV measurement campaign are given in Table 2 and Table 3, respectively. The measured cross-flow sections are perpendicular to the body-fixed longitudinal axis of the W/T model. A number of 13 to 15 sections was measured within the range of $0.125 \leq x / c_r \leq 0.95$, see Fig. 20-2 b). The measurement setup only allows for measurements on the left wing side. The data presented at the right wing side was mirrored from the left wing side. Consequently, the data shown at the right wing side at $\beta = 5 \deg$, was actually measured at the left wing side for $\beta = -5 \deg$.

Table 20-2: Stereo-PIV setup and processing parameters for the first stereo-PIV measurement campaign

Angle between cameras	$60 \deg$	
Image pairs per section	400	
Final field of view	$\approx 0.502 \times 0.250 m^2$	
Number of vectors per section	≈ 21000	
Spatial resolution	$2.42 \cdot 10^{-3} m < \Delta d < 2.63 \cdot 10^{-3} m$	
Non-dimensional spatial resolution	$0.0058 < \Delta d / s < 0.0072$	
Software package	LaVision DaVis 8	
Main algorithm	Stereo cross correlation	
Iteration options	Multipass, decreasing size	
Initial interrogation window	64×64 pixel, 50% overlap, 4 passes	
Final interrogation window	32×32 pixel, 25% overlap, 3 passes	
Configurations and freestream conditions	NA1 W1	NA1 W2
	β = 0 deg, α={16,24,32}deg	β = 0 deg, α={16,24,32}deg

Table 20-3: Stereo-PIV setup and processing parameters for the second stereo-PIV measurement campaign

Angle between cameras	$60\,\mathrm{deg}$	
Image pairs per section	400	
Final field of view	$\approx 0.45 \times 0.210 m^2$	
Number of vectors per section	≈ 45000	
Spatial resolution	$\Delta d = 1.49 \cdot 10^{-3} m$	
Non-dimensional spatial resolution	$3.58 \cdot 10^{-3} < \Delta d / s < 4.07 \cdot 10^{-3}$	
Software package	LaVision DaVis 8	
Main algorithm	Stereo cross correlation	
Iteration options	Multipass, decreasing size	
Initial interrogation window	64×64 pixel, 0% overlap, 1 passes	
Final interrogation window	32×32 pixel, 50% overlap, 3 passes	
Configurations and freestream conditions	NA1 W1	NA1 W2
	$\beta = 0$ deg, α=8deg	$\beta = 0$ deg, α=8deg
	$\beta = 5$ deg, α={16,24,32} deg	$\beta = 5$ deg, α={16,24,32} deg

2.5   Oil Flow Visualization

The skin-friction lines on the upper wing surface were visualized by applying a mixture of cosmetic oil and fluorescent color pigments. The oil/pigment mass ratio defines the viscosity of the mixture. Investigations by Buzica and Breitsamter [20] on a low-aspect ratio configuration at comparable freestream velocities indicate an oil/pigment mass ratio of about 2:1 for this type of flows. However, the heterogeneous flowfield exhibiting locally very high skin friction (e.g. underneath the primary vortex axes) and very low skin friction (e.g. secondary/tertiary structures) makes it difficult to visualize all surface flow structures with the application of a homogeneous mixture on the complete wing surface. The final oil/pigment mass ratios are in the area of 5:1 to 2:1. The mixture of high viscosity was applied at the majority of the wing, whereas the low viscosity mixture was applied near the leading edge and in some local areas at the rear wing section. The wind tunnel model covered with the mixture was exposed to the freestream for approximately 60 seconds. This time was sufficient to obtain converged oil flow patterns on the wing surface. The arising flow skin friction patterns were captured with a digital camera under black light conditions. To avoid too large accumulations of the oil along the separation lines, especially, in the more downstream area of the wing, the measurement was performed in two steps. In the first step, only the rear wing section was covered with the mixture and exposed to the freestream. In the second step, the front wing section was then covered with the mixture as well and the model was again exposed to the freestream. The wing of the NA1 W1 configuration was covered by a glossy black foil with a thickness of about 100 μm to obtain better contrast between the mixture and the metallic wing surface. Examples of the resulting patterns for both configurations (NA1 W1 coated, NA1 W2 uncoated) are illustrated in Fig. 20-3.
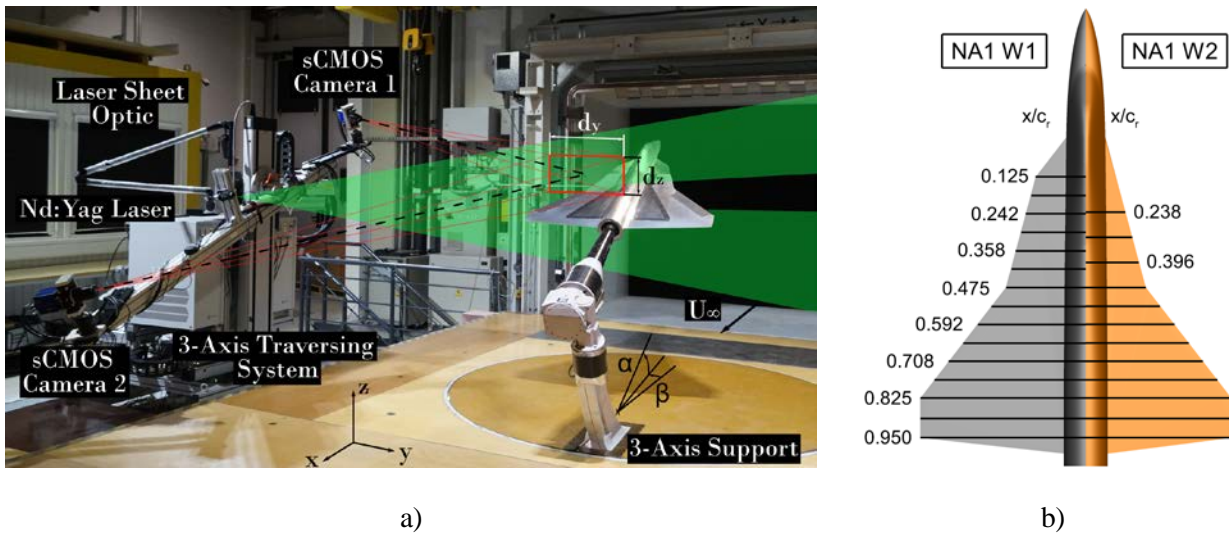
a)   b)

Figure 20-2: (a) Stereo-PIV measurement setup and (b) measured cross-flow sections.

a) NA1 W1 (coated)   b) NA1 W2 (uncoated)
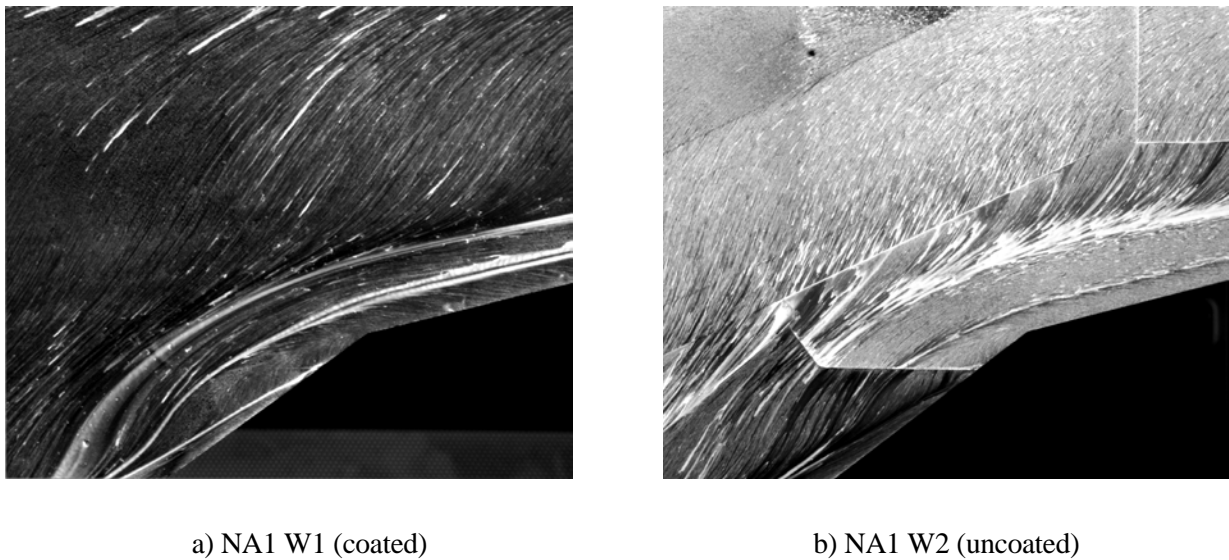
Figure 20-3: Exemplary detail views of the flow skin friction patterns obtained by the oil flow measurements.

3.0 FLOWFIELD ANALYSIS

3.1 Flowfield

The flowfield is shown in Fig. 20-4 and Fig. 20-5 for the NA1 W1 and NA1 W2 configurations at $\beta = 0\,\mathrm{deg}$ and $\beta = 5\,\mathrm{deg}$, respectively. Figure 20-4 illustrates the flowfield for the angles of attack $\alpha = \{8\,\mathrm{deg}, 16\,\mathrm{deg}, 24\,\mathrm{deg}, 32\,\mathrm{deg}\}$ and Fig. 20-5 for $\alpha = \{16\,\mathrm{deg}, 24\,\mathrm{deg}, 32\,\mathrm{deg}\}$. The figures depict the nondimensional axial vorticity for $|\omega_x l_\mu / U_\infty| > 10$ and two different unicolored flow areas. The areas colored in pink indicate the retarded flow areas with $u / U_\infty < 0.2$ and the black colored surfaces indicated the areas of flow reversal with $u / U_\infty < 0$.

3.1.1 Symmetric Freestream Conditions

The flowfield around both the NA1 W1 and NA1 W2 configurations is dominated by two primary leading-edge vortices at each wing side. The first leading-edge vortex develops at the most inboard wing section and is called inboard vortex (IBV). The second leading-edge vortex develops at the kink from the highly swept to the medium swept wing section at $x / c_r = 0.475$ and is called midboard vortex (MBV), see Fig. 20-4. The presented angles of attack outline the different stages of vortex interaction between the IBV and the MBV, see also Ref. [21].

At $\alpha = 8\,\mathrm{deg}$, the IBV and the MBV do not show a considerable interaction, cf. Figs. 20-4 a) and 20-4 e). Both the IBV and the MBV, exhibit a secondary structure indicated by the negative axial vorticity just outboard of the IBV and the MBV. The secondary structure of the IBV is more pronounced in the rear wing area for the NA1 W2 configuration. The decreasing axial vorticity in the IBV in the rear wing section of the NA1 W1 configuration indicates the bursting of the IBV. In this area, the transition from a jet-type to a wake-type axial core flow takes place. Therefore, the induced cross-flow velocities in the outboard direction at the wing surface decrease. This entails lower adverse lateral pressure gradients and consequently a different flow separation characteristic. This results in a less pronounced secondary structure of the IBV for the NA1 W1 configuration. Nevertheless, although the IBV bursts, there are still significant axial vorticity levels observed because the vorticity only slightly decreases in downstream direction. This is a typical vortex bursting behaviour of vortices developing at medium swept leading edges, cf. Ref. [4].

At $\alpha = 16\,\mathrm{deg}$, a strong vortex interaction and considerable differences between the NA1 W1 and NA1 W2 configurations are observed, see Figs. 20-4 b) and 20-4 f). For the NA1 W1 configuration, the MBV is immediately moved away from the surface downstream of its development onset. The MBV is moved upward and inward, whereas the IBV is moved outward. However, due to the breakdown of the IBV, the interaction of the IBV and the MBV becomes weaker downstream of the IBV breakdown location. Compared to $\alpha = 8\,\mathrm{deg}$, the IBV bursting onset is further upstream at $x / c_r \approx 0.475$. The vorticity constantly decreases in downstream direction. Near the wing trailing edge, there is also the typical consequence of vortex bursting observed in form of a reverse flow. The NA1 W2 configuration, in contrast, exhibits a stable vortex system consisting of the IBV and the MBV with a strong vortex interaction over the wing. Both vortices show a distinct rotation around each other. The system of stable and interacting IBV and MBV stays close to the wing surface.
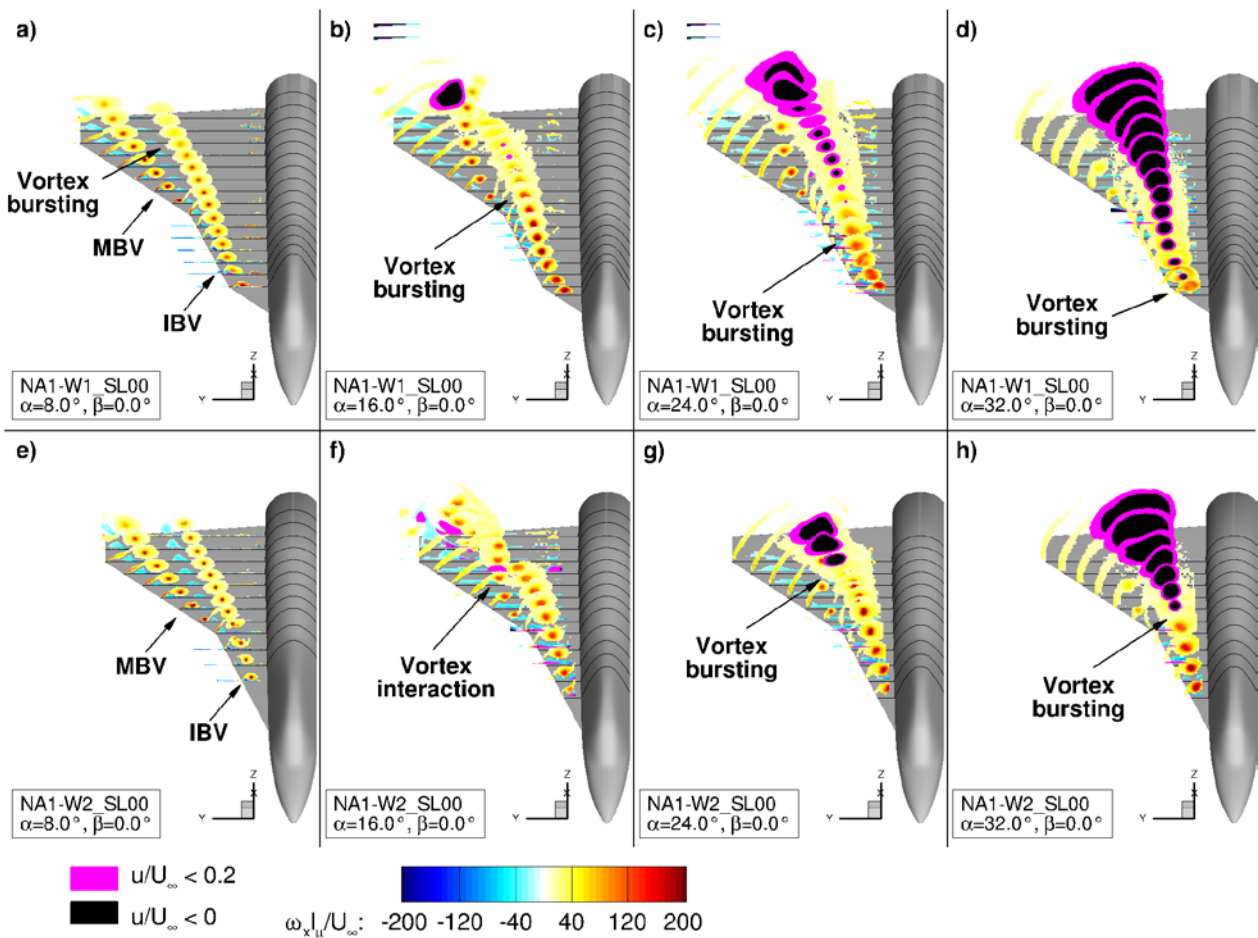
Figure 20-4: Nondimensional axial vorticity and axial velocity distributions of the NA1 W1 and NA1 W2 configurations at different α and β = 0 deg.

With the angle of attack increasing to $\alpha = 24\,\mathrm{deg}$, the IBV bursting onset at the NA1 W1 configuration moves further upstream. A reverse flow is present at $x/c_r \approx 0.475$, see Fig. 20-4 c). The cross sections indicating the retarded and reverse flow are constantly increasing in downstream direction. The axial vorticity in the vortex core decreases, however, there is still considerable vorticity present in the burst vortex. The NA1 W2 configuration now also shows vortex bursting over the wing. There, the axial vorticity abruptly decreases, the vortex cross section increases and the flow is immediately decelerated to a reverse flow. Similar to the NA1 W1 configuration, the vortex interaction is now significantly weakened. The MBV is now also moved away from the wing surface but no pronounced rotation of the IBV and the MBV around each other is observed due to the IBV bursting. The differences in the IBV bursting characteristics are associated with the leading-edge sweep at the inboard section of the NA1 W1 and NA1 W2 configurations. At the NA1 W1 configuration, the IBV develops at a non-slender wing section. At the NA1 W2 configuration, the IBV develops at a slender wing section. This results in the different vortex breakdown behaviour and in the bursting occurring at higher angles of attack for the NA1 W2 configuration.

A further increase of the angle of attack to $\alpha = 32\,\mathrm{deg}$ shows the expected characteristics of a further upstream vortex bursting onset at both configurations, cf. Figs. 20-4 d) and h). The vortex interaction is of the same type as for $\alpha = 24\,\mathrm{deg}$. The MBV is moved away from the wing surface and stays separated from the wing.

3.1.2 Sideslip Angle Conditions

Figure 20-5 depicts the flowfield at $\beta = 5\,\text{deg}$. The flow direction is from the lower left to the upper right as it is indicated by the arrow in each subfigure.

At $\alpha = 16\,\text{deg}$, the asymmetry in the flowfield of the NA1 W1 configuration due to the angle of sideslip can be observed, especially, at the rear wing section, see Fig. 20-5 a). At the windward side, the IBV bursts at $x/c_r \approx 0.475$, which is indicated by the reduction in the axial vorticity and a slight increase in the IBV cross section. However, no area of flow reversal is observed. The vortex interaction is similar as it is observed for the symmetric freestream condition at the same angle of attack, cf. Fig. 20-4 b). At the leeward side, however, the vortices do not burst. The interaction between the IBV and the MBV is stronger than at the windward side, resulting in a more progressed rotation of the IBV and the MBV around each other. The interaction is comparable to the one observed at $\alpha = 16\,\text{deg}$ and $\beta = 0\,\text{deg}$ for the NA1 W2 configuration, cf. Fig. 20-4 f). The NA1 W2 configuration exhibits a completely stable vortex system at the leeward side, see Fig. 20-5 b). The interaction is similar to the one observed at $\alpha = 16\,\text{deg}$ and $\beta = 0\,\text{deg}$, cf. Fig. 20-4 f). At the windward side, the IBV bursts near the wing trailing edge. Up to this location, the IBV and the MBV show a strong interaction with a pronounced rotation around each other. The bursting entails a strong increase in the vortex cross section and a large area of reverse flow, but does not affect the vortex interaction upstream.

The asymmetry in the flowfield significantly increases for $\alpha = 24\,\text{deg}$, see Figs. 20-5 c) and d). The NA1 W1 configuration features an almost completely stable vortex system at the leeward side, see Fig. 20-5 c). The small area of reverse flow close to the wing trailing edge indicates the beginning of the IBV bursting over the wing. The interaction between the IBV and the MBV is slightly diminished. The vortex interaction causes the MBV to move away from the wing surface, but the rotation is not strong enough to bring the MBV back to the wing surface until it crosses the wing trailing edge. At the windward side in contrast, the vortex bursting onset has almost reached the wing apex. Similar to the observations at $\beta = 0\,\text{deg}$, the vortex bursting takes place in a less sudden way than at slender delta wings. There are still considerable vorticity levels observable up to $x/c_r \approx 0.475$. The NA1 W2 configuration shows a comparable picture, cf. Fig. 20-5 d). The vortex system on the leeward side is stable, presenting a thorough rotation of the IBV and the MBV around each other. The vortex bursting on the windward side is now observed at $x/c_r \approx 0.475$ and thus considerably more downstream than for the NA1 W1 configuration, compare Figs. 20-5 d) and c). The bursting entails the abrupt reduction of vorticity, the increase in the vortex cross section and a large area of reverse flow. The vortex interaction at the windward side is thus comparable with the one at $\alpha = 24\,\text{deg}$ and $\beta = 0\,\text{deg}$, cf. Fig. 20-4 g). At $\alpha = 24\,\text{deg}$ and $\beta = 5\,\text{deg}$, the effect of the angle of sideslip and thus the effect of the increase and decrease of the leading-edge sweep at the leeward and windward wing side, respectively, is very clear. The effective increase of the leading-edge sweep at the leeward side shifts the vortex bursting to higher angles of attack. At the windward side, the opposite effect occurs. Consequently, the vortex bursting at the windward side is observed more upstream than at $\alpha = 24\,\text{deg}$ and $\beta = 0\,\text{deg}$. At the leeward side, there is almost no vortex bursting present, whereas it is present at $\alpha = 24\,\text{deg}$ and $\beta = 0\,\text{deg}$ for both configurations.

At the angle of attack $\alpha = 32\,\text{deg}$, no vortex system is observed at the windward side, see Figs. 20-5 e) and f). The complete wing exhibits irregular flow separation with flow reversal. At the leeward side of the NA1 W1 configuration, the vortex bursting onset of the IVB has moved considerable upstream. As could already be observed at the previous freestream conditions, the IBV bursting is smooth and the vorticity and axial velocity are steadily decreased in downstream direction. At this angle of attack, the leeward side vortex evolving at the fuselage can be observed between the IBV and the fuselage, see Fig. 20-5 e). The NA1 W2

configuration still exhibits a stable vortex system at the leeward side, see Fig. 20-5 f). The leeward fuselage vortex is also visible, however, due to the smaller local wing span of the NA1 W2 configuration, the fuselage vortex is not that pronounced as for the NA1 W1 configuration.
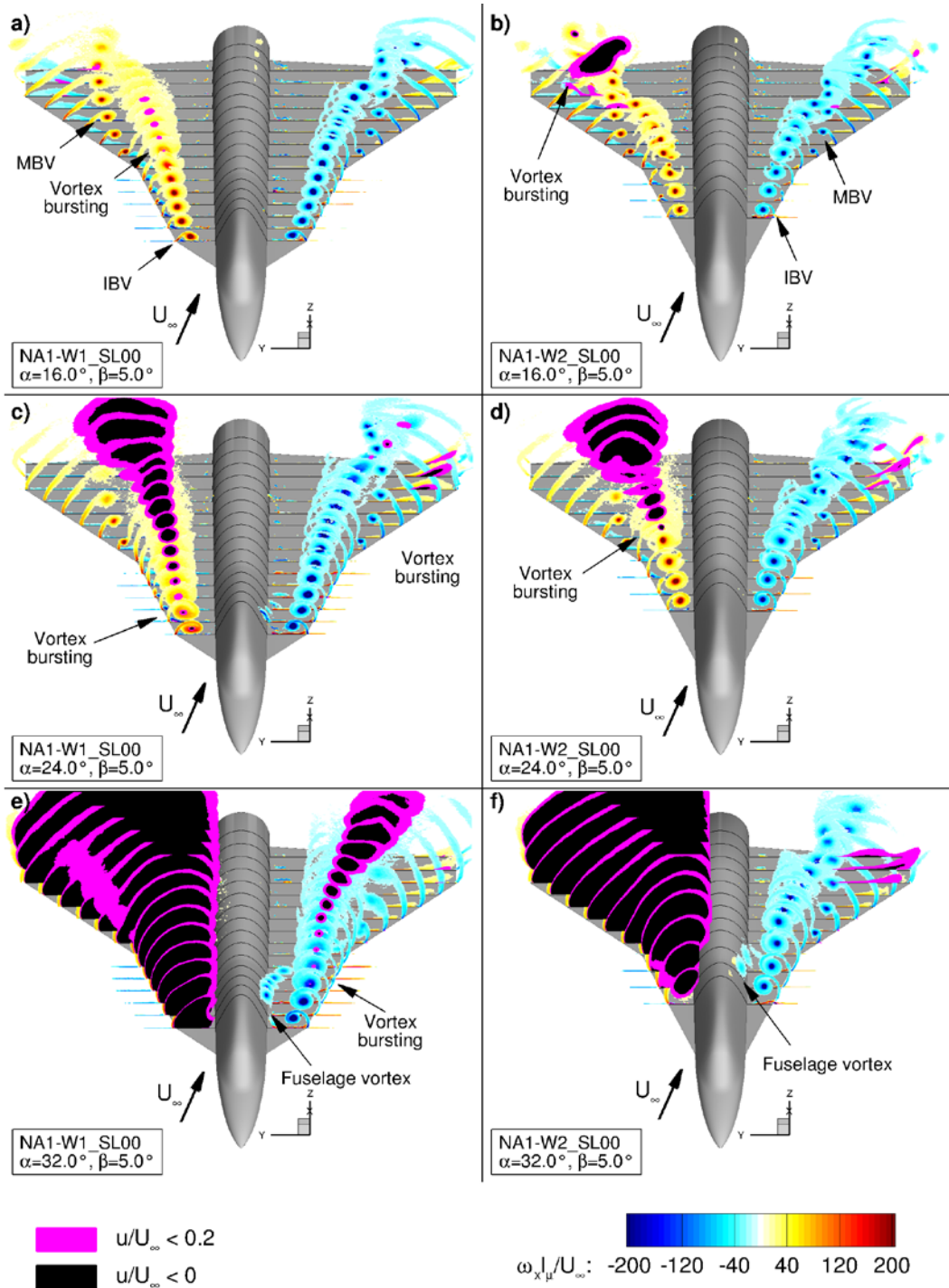

Figure 20-5: Nondimensional axial vorticity and axial velocity distributions of the NA1 W1 and NA1 W2 configurations at different α and β = 5 deg.

3.2 Vortex Breakdown

The vortex breakdown locations on the NA1 W1 and NA1 W2 configurations for the symmetric freestream conditions are discussed in the following, see also Ref. [21]. Figure 20-6 shows the breakdown positions of the IBV and the MBV for the NA1 W1 and NA1 W2 configurations for $\alpha = \{16\,\text{deg}, 24\,\text{deg}, 32\,\text{deg}\}$ at $\beta = 0\,\text{deg}$. The vortex bursting locations are determined differently for the vortices evolving at a slender (NA1 W2 IBV) or a non-slender wing section (IBV and MBV NA1 W1, MBV NA1 W2). For the vortices developing at a slender wing section, the vortex breakdown is determined by the first appearance of a reverse flow. The vortex breakdown location of the vortices developing at a non-slender wing section is determined by the transition from a jet type to a wake type axial core flow, cf. Ref. [4]. Additionally, the results of Wentz and Kohlman [5] for pure delta wings of comparable leading-edge sweep are illustrated in Fig. 20-6. The investigations of Wentz and Kohlman were performed on pure delta wings without a fuselage. They are, therefore, not directly comparable, but give a good indication on where the vortex breakdown is to be expected.
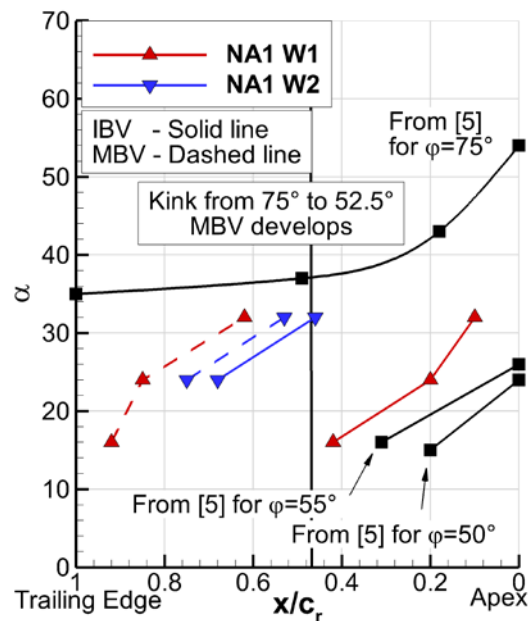
Figure 20-6: Vortex-breakdown locations relative to root chord dependent on α for the NA1 W1 and NA1 W2 configurations. Includes data taken from Ref. [5]. Modified, based on [21].

The IBV of the NA1 W1 configuration bursts at $x/c_r \approx 0.45$ for $\alpha = 16\,\text{deg}$. With the angle of attack increasing, the vortex breakdown location moves upstream to $x/c_r \approx 0.1$ at $\alpha = 32\,\text{deg}$. Compared to the values from the literature, the vortex breaks down more downstream. This can be associated with the change of the wing sweep from 52.5 deg to 75 deg at $x/c_r \approx 0.125$. At $\alpha = 16\,\text{deg}$, the MBV breakdown location is observed at $x/c_r \approx 0.92$. Consequently, the MBV bursts after an effective length of $\Delta x/c_r \approx 0.45$. This is comparable to the breakdown of the IBV. Since the MBV develops along a constantly swept wing section with a medium wing sweep, the long lifetime of the MBV is likely to be a result of the interaction of the IBV and the MBV. The breakdown location of the MBV moves considerably upstream with an increasing angle of attack. At $\alpha = 32\,\text{deg}$, the MBV travels $\Delta x/c_r \approx 0.1$ before it bursts. The distance

between the IBV and the MBV breakdown onset is $\Delta x / c_r > 0.5$. Thus, the IBV breakdown does not have an immediate destabilizing effect on the MBV.

The NA 1 W2 configuration exhibits a different behaviour. There is no vortex bursting at $\alpha = 16 \deg$, although vortex bursting could be expected for the MBV, since it develops at a 52.5 degree swept wing section. The IBV of the NA1 W2 configuration is much more stable than the IBV of the NA1 W1 configuration due to the increased leading-edge sweep of the inboard wing section. At $\alpha = 24 \deg$ and $\alpha = 32 \deg$, the IBV and the MBV burst over the wing, whereas the vortex bursting onsets move upstream with an increasing angle of attack. Compared to the breakdown at a 75 degree swept delta wing, the breakdown of the IBV is shifted to lower angles of attack. This can be related to the separation of the IBV from the leading-edge shear layer at $x / c_r = 0.475$. The breakdown of the IBV has a direct effect on the stability of the MBV. At $\alpha = 24 \deg$ and $\alpha = 32 \deg$, the MBV breakdown location is $\Delta x / c_r \approx 0.05$ downstream of the IBV breakdown location. The bursting IBV immediately destabilizes the MBV and causes its breakdown. Consequently, the different vortex breakdown behaviour of the IBV on the NA1 W1 and NA1 W2 configurations observed in the flowfield has a direct effect on the stability of the MBV.

3.3 Wall-Near Flow

The surface and wall-near flow is discussed by means of oil flow visualization. Figure 20-7 illustrates skin-friction patterns obtained by the oil flow measurements and the inferred sketches for the NA1 W1 and NA1 W2 configurations at $\alpha = 16 \deg$ and $\beta = 0 \deg$. Curves of different colors are shown in the sketches. The green curves connect local streamlines. Curves of converging streamlines are drawn in red and indicate a flow separation. Lines of diverging streamlines are blue and indicate a flow attachment. The light blue lines indicate the location of a vortex axis.

The skin-friction patterns of the NA1 W1 configuration show the IBV in the inboard wing section by the strongly outboard deflected streamlines. The flow separates at the leading edge and reattaches near the wing root either at the wing surface or at the fuselage. The primary reattachment line in the front wing section is not clearly recognizable in the oil flow patterns and is, thus, not included in the sketch. The outboard deflected streamlines exhibit an inflection point indicating the location of the vortex axis. Near the leading edge, the streamlines converge, which results in the secondary separation line of the IBV. The flow reattaches outboard of the secondary separation line near the leading edge. The IBV moves downstream along the medium swept leading-edge in the inboard wing section. This results in considerable less deflected streamlines in the inboard wing section. At some point on the highly swept midboard wing section, a tertiary structure occurs inside the secondary structure near the leading edge. It is represented by another pair of convergence and divergence line representing the tertiary separation and reattachment lines, respectively. The tertiary structure is very small and associated with very low skin friction values, which makes it difficult to recognize, especially, the reattachment line. Consequently, the exact onset of the tertiary structure cannot be determined from the available oil flow patterns. Complementary numerical simulations at $\alpha = 24 \deg$ also show a third pair of divergence and convergence line near the leading edge. The associated structure is very small and has a vertical extension in the order of the boundary layer thickness. In the numerical simulations it is not represented as a vortex structure. Additional investigations on the details of the tertiary structure would be necessary for further insight. At the kink from the midboard to the outboard wing section at $x / c_r = 0.475$, the reattachment line of the secondary structure is not deflected outboard and does, thus, not follow the leading-edge. Outboard of the secondary reattachment line, the streamlines are strongly deflected in outboard direction and another separation line (MBV – Secondary Separation) and reattachment line (MBV – Secondary Reattachment) can be observed. This is seen to be the effect of the developing MBV, which induces high cross-flow velocities near the wing surface. The IBV secondary reattachment line is not recognizable anymore shortly downstream of the MBV development onset and the IBV tertiary

separation line merges with the MBV secondary separation line. This represents the MBV moving away from the wing surface by its interaction with the IBV. The bursting of the IBV results in less deflected streamlines in the midboard wing area. Downstream of the kink at $x/c_r = 0.475$, no clear convergence of the streamlines into the IBV secondary separation line is observed. The divergence line becomes a dividing streamline and merges with the MBV secondary separation line. Furthermore, the primary reattachment line is observable near the wing root in the oil flow patterns, since the vortex system moves in outboard direction.
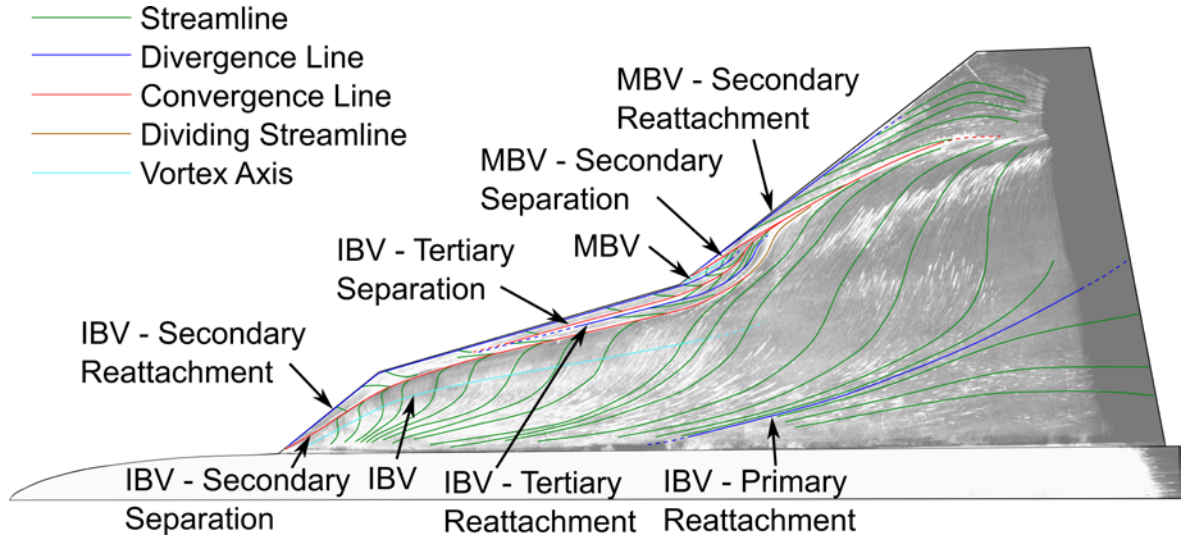
a) NA1 W1
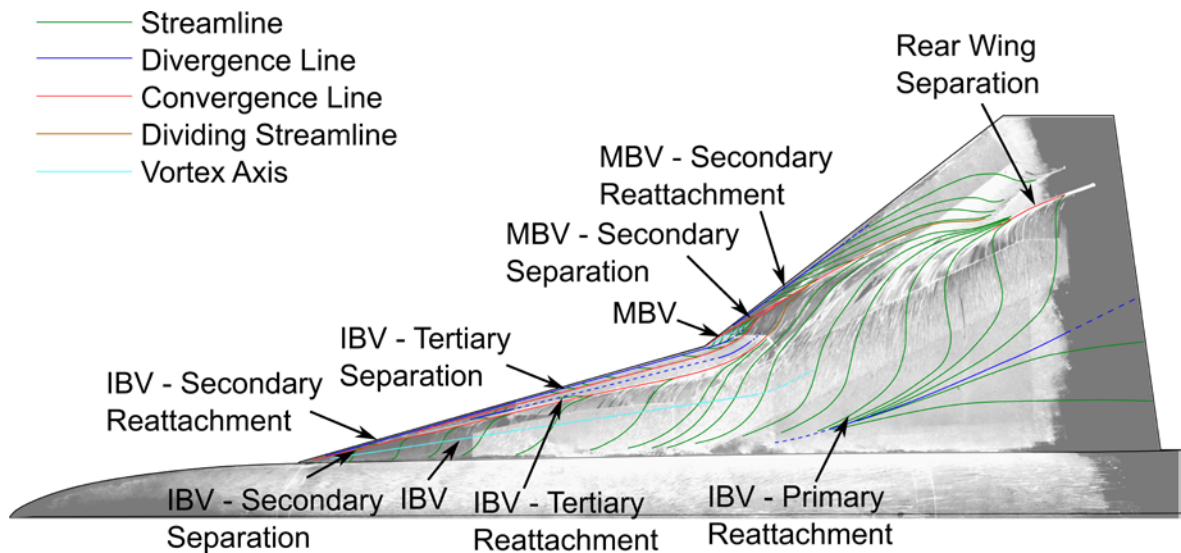
b) NA1 W2

Figure 20-7: Oil flow picture and inferred wall stream lines for the NA1 W1 and NA1 W2 configurations at α=16 deg and β=0 deg.

The NA1 W2 configuration shows a comparable picture, see Fig. 20-7 b). At the inboard wing section, the curved streamlines underneath the IBV and a secondary and tertiary structure are present. At the kink at $x/c_r = 0.475$, the additional convergence and divergence lines due to the MBV can be observed. The merging of the IBV tertiary and secondary separation line with the MBV secondary separation line indicate the separation of the MBV from the wing surface due to the interaction with the IBV. For the NA1 W2 configuration, the streamlines in the rear wing section are significantly deflected in outboard direction due to the completely stable vortex system and the proximity of the vortices to the wing surface. The streamlines diverging from the IBV primary attachment line are converging in a further separation line in the rear wing area. Thereby, the streamlines emanating from the IBV primary reattachment line more upstream are approaching the separation line from the outboard direction. The streamlines emanating more downstream from the IBV primary reattachment line are approaching the rear wing separation line from the inboard direction. Additionally, the streamlines emanating from the MBV secondary reattachment line are converging into the rear wing separation line.

4.0   PERFORMANCE AND STABILITY CHARACTERISTICS

The longitudinal and lateral performance and stability characteristics are presented in the following sections. The results from section 3.1 are utilized to associate the performance and stability characteristics with the flow-physical phenomena occurring at the configurations, see also Ref. [21].

4.1   Longitudinal Characteristics

The performance and stability characteristics of the longitudinal motion are discussed by means of the lift coefficient polars and the pitching moment coefficient polars. Figure 20-8 a) illustrates the lift coefficient versus the angle of attack for the NA1 W1 and NA1 W2 configurations at $\beta = 0\,\text{deg}$ and $\beta = 5\,\text{deg}$.

Both configurations exhibit the same characteristic up to an angle of attack of $\alpha \approx 13\,\text{deg}$. For $\alpha > 6\,\text{deg}$, the additional non-linear vortex lift can be observed for both configurations and angles of sideslip. The lift of the NA1 W1 configuration at $\beta = 0\,\text{deg}$ shows a slight and continuous decrease of the slope at $\alpha \approx 15\,\text{deg}$. At this point, the IBV bursting affects the lift. As it was described, the vortex bursting entails a reduction of the axial vorticity. A reduced axial vorticity indicates reduced cross-flow velocities, which are responsible for the vortex induced suction at the wing upper side. The smooth vortex bursting with its constant reduction of the axial vorticity in downstream direction causes the smooth decrease of the lift slope. With the angle of attack increasing, the lift constantly increases up to $\alpha_{\text{max}} = 33\,\text{deg}$ with a maximum lift coefficient of $C_{L,\text{max}} = 1.5$. The lift polar of the NA1 W1 configuration at $\beta = 0\,\text{deg}$ indicates an uncritical and smooth transition into the post-stall regime. The lift polar of the NA1 W1 configuration at $\beta = 5\,\text{deg}$ shows a comparable picture with minor differences. The effect of the IBV bursting appears at slightly higher angles of attack and the stall is observed at slightly lower angles of attack. The maximum α is, however, at a higher angle of attack of $\alpha_{\text{max}} = 36\,\text{deg}$. The maximum lift at $\beta = 5\,\text{deg}$ reads $C_{L,\text{max}} = 1.4$ and is thus lower than at $\beta = 0\,\text{deg}$.

The NA1 W2 configuration shows a sudden, short-term reduction of the lift at an angle of attack of $\alpha = 23\,\text{deg}$ for $\beta = 0\,\text{deg}$ and at $\alpha = 19\,\text{deg}$ for $\beta = 5\,\text{deg}$. This effect is associated with the bursting of the IBV and its effect on the MBV. At $\alpha = 16\,\text{deg}$ and $\beta = 0\,\text{deg}$, the NA1 W2 configuration features a completely stable vortex system with a pronounced rotation of the IBV and the MBV around each other, see Fig. 20-4 f).

a) Lift coefficient C_L b) Pitching moment coefficient C_{my}
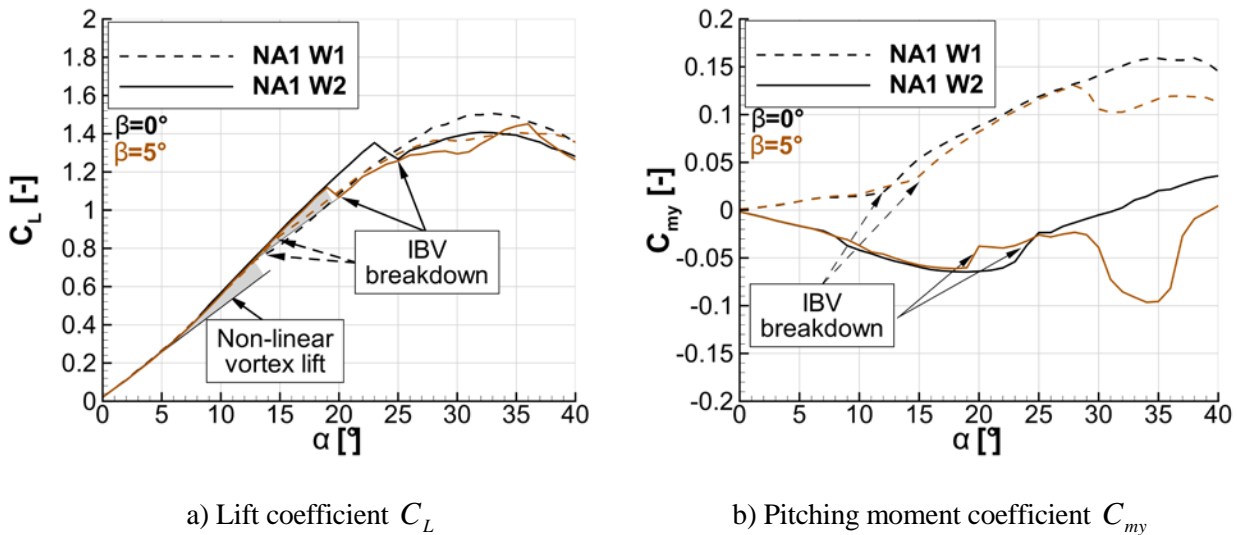
Figure 20-8: Longitudinal aerodynamic coefficients for the NA1 W1 and NA1 W2 configurations versus α at $\beta = 0 \deg$ and $\beta = 5 \deg$.

Both vortices stay close to the wing surface and are thus able to induce suction at the wing upper side. At $\alpha = 24 \deg$ and $\beta = 0 \deg$, the IBV bursts and the vortex interaction changes, with the MBV staying separated from the wing surface, see Fig. 20-4 g) . Furthermore, the IBV bursting entails the abrupt reduction of the axial vorticity. At $\alpha = 16 \deg$ and $\beta = 5 \deg$, the windward side shows the state of the vortex system shortly before the discontinuity in the lift polar occurs, see Fig. 20-5 b). The IBV bursts in the rear wing section, but does not affect the strong vortex interaction yet. A slight increase in the angle of attack then entails the upstream motion of the vortex bursting onset resulting in a very different flowfield, as it is seen in Fig. 20-4 g). The lift polar indicates, that the change from the stable, strongly interacting vortex system to the unstable, less pronounced interacting vortex system happens abruptly. The maximum angle of attack at $\beta = 0 \deg$ reads $\alpha_{\max} = 33 \deg$ with a maximum lift of $C_{L,\max} = 1.41$. At $\beta = 5 \deg$, the maximum angle of attack reads $\alpha_{\max} = 36 \deg$ with a maximum lift of $C_{L,\max} = 1.45$.

Figure 20-8 b) illustrates the pitching moment polars for the NA1 W1 and NA1 W2 configurations at $\beta = 0 \deg$ and $\beta = 5 \deg$. The NA1 W1 configuration exhibits an increasing pitching moment with the angle of attack, indicating a static longitudinal unstable behaviour with respect to the chosen moment reference point. A local pitch-up tendency can be seen for $\beta = 0 \deg$ and $\beta = 5 \deg$ at the same angles of attack, where the lift slope decreases, cf. Fig. 20-8 a). The local pitch-up tendency is related to the IBV bursting taking place above the wing. For $\beta = 0 \deg$, the pitching moment increases up to the stall and slightly decreases in the post-stall region. For $\beta = 5 \deg$, the pitching moment exhibits a local pitch-down tendency at $\alpha \approx 28 \deg$. At that point, the IBV bursting at the windward side approaches the wing apex and the flow structure changes to an irregular flow separation with flow reversal. Consequently, the lift produced in the front wing section is considerably reduced at the windward side. The vortex breakdown onset at the leeward side is still enough downstream so that suction is induced in the rear wing section. With a further upstream motion of the vortex bursting onset at the leeward side, the pitching moment again increases up to $\alpha = 37 \deg$.

Compared to the NA1 W1 configuration, the pitching moment of the NA1 W2 configuration decreases with an increasing angle of attack for low to medium α. This indicates a static longitudinal stability with respect to

the chosen reference point. This is related to the different wing planforms. The larger local span in the front wing section of the NA1 W1 configuration results in the different pitching moment tendency. Similar to the lift polar characteristic, the pitching moment shows an abrupt pitch-up tendency at $\alpha = 24\deg$ for $\beta = 0\deg$ and at $\alpha = 19\deg$ for $\beta = 5\deg$. This is related to the IBV breakdown. The breakdown decreases the lift in the rear wing section resulting in the pitch-up tendency. With increasing angle of attack, the pitching moment increases due to the upstream motion of the vortex bursting onset and the increasing strength of the IBV in the inboard wing section. For $\beta = 5\deg$, the pitching moment exhibits a local pitch-down tendency at $\alpha \approx 29\deg$. Similar to the NA1 W1 configuration, the bursting onset at the windward side approaches the wing apex. At the leeward side, the vortex system is still stable and thus inducing high suction also in the rear wing section. With an increasing angle of attack, the leeward side vortex system also bursts above the wing, which results in another strong pitch-up tendency at $\alpha = 36\deg$.

4.2   Lateral and Directional Characteristics

The characteristics of the lateral and directional motions are determined by the rolling moment coefficient C_{mx} and the yawing moment coefficient C_{mz}. A positive rolling moment coefficient indicates a right wing down rotation of the aircraft, and a positive yawing moment coefficient indicates a nose right rotation of the aircraft. With respect to the stability analysis, the derivatives of the coefficients with respect to the angle of sideslip are of interest. The derivatives are defined as $C_{mi\beta} = dC_{mi} / d\beta$. The lateral stability parameter $C_{mx\beta}$ indicates a stable behaviour for $C_{mx\beta} < 0$ and the directional stability parameter indicates a stable behaviour for $C_{mz\beta} > 0$. An arising instability is thus observable by a change in the sign of the stability parameter. High-performance aircraft typically exhibit a so-called roll reversal ($C_{mx\beta}$ instability) and directional divergence ($C_{mz\beta}$ instability) at a certain angle of attack, cf. Ref. [10]. Tests at the NASA Langley Research Center free flight tunnel showed that a directional divergence can also appear although both steady stability parameters indicate a stable behaviour [9,10]. It was shown, that a certain combination of the lateral and directional stability parameters and the moment-of-inertia ratio I_Z / I_X causes the directional divergence. They derived a formulation predicting the actual divergence characteristic fairly well on the basis of steady aerodynamic data [9,10]. The parameter is called dynamic directional stability parameter and is defined as

$$C_{mz\beta,dyn} = C_{mz\beta} \cos\alpha - \frac{I_Z}{I_X} C_{mx\beta} \sin\alpha \ .$$

One needs to be aware that this formulation is based on the linearized equations of motion, assumes a linear characteristic of $C_{mx\beta}$ and $C_{mz\beta}$, and does not account for possible variations in the dynamic derivatives. Consequently, the formulation might not be valid in the high angle of attack regime. The detailed investigations by Greer [10], however, confirm the applicability of the derived formulation for low-aspect-ratio configurations. The evaluation of the dynamic directional stability parameter requires the moment-of-inertia ratio I_Z/I_X. The moment-of-inertia ratio was defined by the data available in Ref. [22] for a full-scale delta wing-body configuration of an aircraft with comparable leading-edge sweep and wing aspect ratio. The same value is applied for both configuration and is given in Tab. 1.
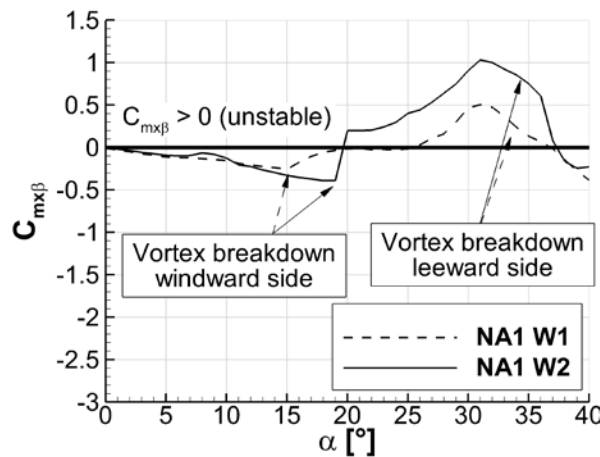
Figure 20-9 a) depicts the lateral stability parameter versus the angle of attack at $\beta = 0\deg$ for the NA1 W1 and NA1 W2 configurations. Both the NA1 W1 and NA1 W2 configurations feature a stable behaviour in the low to medium angle-of-attack regime. The NA1 W1 configuration has its maximum stability at $\alpha = 15\deg$. Up to this angle of attack, the vortex system on both wing sides is stable. The lower effective

wing sweep at the windward side at sideslip conditions results in a higher lift at the windward side than at the leeward side and, thus, in a stable rolling moment, cf. Hummel et al. [6]. However, the lower effective wing sweep also results in a vortex bursting at lower angles of attack, cf. Wentz and Kohlman [5]. This effect is observable for $\alpha > 15\,\mathrm{deg}$. The values of the lateral stability parameter approach zero at $\alpha \approx 20\,\mathrm{deg}$. This is associated with the IBV bursting on the windward side, see Fig. 20-5 c). The reduced vortex interaction and vorticity results in lower suction and, thus, in a reduced lift. Consequently, the rolling moment changes. However, since the vortex bursting is smooth and associated with considerable vorticity in the wake of the burst IBV, there is still enough lift generated at the windward side to avoid a clear roll reversal up to an angle of attack of $\alpha = 25\,\mathrm{deg}$. In addition to the vortex bursting characteristics at the windward side, the vortex system at the leeward side also becomes unstable at $\alpha \approx 25\,\mathrm{deg}$. This results in the attenuated roll reversal. The vortex bursting onset moves upstream and the lift generated at the leeward side decreases. The maximum instability is observed at $\alpha = 32\,\mathrm{deg}$. There, the vortex system at the windward side is not present anymore but an area of irregular flow separation with reverse flow is observed, cf. Fig. 20-5 e). At the leeward side, the bursting onset moves further upstream, which results in a reduction of the lateral stability parameter.
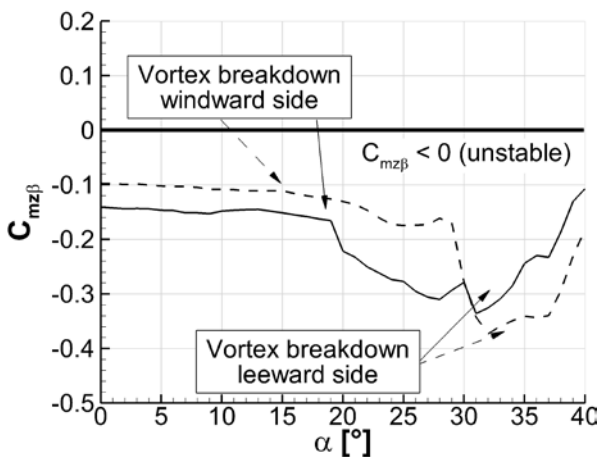
The lateral stability parameter of the NA1 W2 configuration shows a characteristic consistent with the flowfield and the longitudinal stability and performance characteristics. A lateral stability is given for $\alpha \leq 19\,\mathrm{deg}$. Although the flowfield shows bursting of the vortex system near the wing trailing edge at the windward side, it does not result in a significant lift reduction and, thus, no roll reversal is seen. For $\alpha > 19\,\mathrm{deg}$, however, the windward side vortex system abruptly breaks down. The breakdown changes the vortex interaction, with the MBV being moved away from the wing surface and breaking down shortly downstream of the IBV, cf. Figs. 20-5 d) and 20-6. Downstream of the IBV bursting location, the induced lift is considerably decreased. The abrupt occasion and the effects of the vortex bursting on the vortex interaction result in the sudden roll reversal at $\alpha = 20\,\mathrm{deg}$. Due to the upstream motion of the vortex bursting onset at the windward side and the stability of the vortex system at the leeward side, the instability increases up to $\alpha = 31\,\mathrm{deg}$. At this angle of attack, the vortex system at the windward side is not present anymore and the vortex system at the leeward side is still stable. This maximum asymmetry in the flowfield results in the most unstable condition. With an increase in the angle of attack, the vortex system at the leeward side starts to burst, which reduces the lift at the leeward side and, thus, alleviates the lateral instability. Due to the maximum asymmetry on the NA1 W2 configuration at $\alpha \approx 32\,\mathrm{deg}$, with irregular separated flow at the windward side and a completely stable vortex system at the leeward side the absolute value of the instability is significantly higher than for the NA1 W1 configuration. There, the vortex system at the leeward side starts to burst at an angle of attack where the vortex system at the windward side still exists. This effect is, in combination with the different bursting characteristic, responsible for the smoother transition from stable to unstable for the NA1 W1 configuration. The onset of the instability, however, is at lower angles of attack for the NA1 W1 configuration than for the NA1 W2 configuration due to the development of the IBV at the non-slender wing section.

Figure 20-9 b) illustrates the directional stability parameter versus the angle of attack for the NA1 W1 and the NA1 W2 configurations. Both configurations exhibit a directional instability for the considered angle of attack range. In the low angle of attack range, the major contribution to the directional instability is likely to be related to the fuselage front area including the canopy. With increasing angle of attack, the vortex bursting at the windward side further increases the instability, which shows a maximum in the same angle of attack range as the lateral stability for both configurations. The vortex bursting at the windward side results in a decreased lift and thus also in a decreased lift induced drag, which results in a destabilizing yawing moment. The reduction of the instability at higher angles of attack can then be related to the breakdown of the vortex system at the leeward side. In general, the absolute values of the directional stability parameter are considerably lower than of the lateral stability parameter.
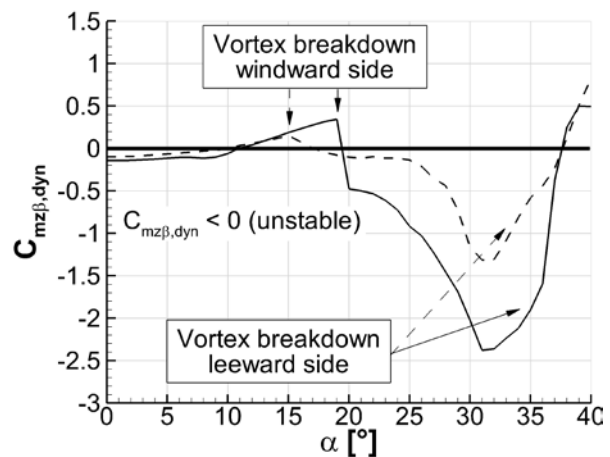
Figure 20-9 c) depicts the dynamic directional stability parameter versus the angle of attack of the NA1 W1 and NA1 W2 configurations. Basically, the same characteristics as previously described for the lateral and directional stability parameters are present. In the low angle of attack regime, a slightly unstable behaviour because of the directional instability is observed, which dominates in the low angle of attack range. With increasing angle of attack, the lateral stability parameter becomes more dominant in the dynamic directional stability. This results in a small angle of attack range exhibiting stable behaviour for both configurations. The arising instability for the NA1 W1 configuration for $\alpha > 17\,\mathrm{deg}$ and for the NA1 W2 configuration for $\alpha > 19\,\mathrm{deg}$ shows the same characteristics as the lateral stability parameters and are related to the same flow phenomena. The consideration of the moment-of-inertia ratio leads to remarkably higher values of the dynamic stability parameter in comparison to the steady stability parameters.

a) Lateral stability parameter $C_{mx\beta}$

b) Directional stability parameter $C_{mz\beta}$

c) Dynamic directional stability parameter $C_{mz\beta,dyn}$

Figure 20-9: Directional and lateral stability parameters for the NA1 W1 and NA1 W2 configurations versus α at $\beta = 0\,\mathrm{deg}$.

5.0   CONCLUSION

The flowfield and the longitudinal, lateral, and directional flight physical stability characteristics of a generic low-aspect-ratio multiple-swept wing fuselage configuration have been presented. The experiments were performed at low subsonic conditions at symmetric and asymmetric freestream conditions.

The flowfields of both the NA1 W1 and NA1 W2 configurations are dominated by the interacting vortex system consisting of the inboard vortex and the midboard vortex. The inboard vortex develops at the inboard wing section, which differs for both configurations. The NA1 W1 configuration exhibits a medium swept inboard wing section and the NA1 W2 configuration a highly swept inboard wing section. The leading-edge sweep of the inboard wing section significantly influences the vortex breakdown behaviour of the inboard vortex in the sense of vortex bursting onset (at higher or lower α) and abruptness (abrupt or smooth vortex bursting) of the vortex breakdown. The breakdown of the inboard vortex at the NA1 W2 configuration takes place at higher angles of attack than at the NA1 W1 configuration, but more abrupt with an immediate adverse effect on the midboard vortex stability. At high angles of attack, the NA1 W2 configuration shows a maximum possible asymmetry at sideslip conditions with a complete irregular flow separation with flow reversal at the windward side and a completely stable vortex system at the leeward side.

Both configurations feature longitudinal, lateral and directional instabilities. The NA1 W2 configuration exhibit strong instabilities due to the large asymmetry in the flowfield at high α. The abrupt vortex bursting of the inboard vortex and its effect on the vortex interaction patterns result in critical instability onsets with abrupt instabilities arising within few degree angle of attack. For the NA1 W1 configuration, the maximum instabilities as well as the onsets are significantly alleviated in comparison to the NA1 W2 configuration. This is associated with the smooth vortex bursting characteristic and its effect on the vortex interaction. Thereby, the alleviated flight mechanics instability characteristic are not gained by a stabilization of the windward vortex system. It is gained by a slightly reduced stability of the leeward vortex system, which is, however, related to less abrupt vortex bursting characteristics. This alleviates the asymmetry in the flowfield at high angles of attack and smoothens the transition from a stable to an unstable condition. The NA1 W1 configuration is, therefore, a good basis for the further investigation on improved stability characteristics by means of wing planform triggered vortex systems.

Acknowledgements

BIBLIOGRAPHIE

[1]   Breitsamter, C., "Unsteady Flow Phenomena Associated with Leading-Edge Vortices," Progress in Aerospace Sciences, Vol. 44, No. 1, 2008, pp. 48–65. doi:10.1016/j.paerosci.2007.10.002.

[2]   Gursul, I., "Review of Unsteady Vortex Flows over Slender Delta Wings," Journal of Aircraft, Vol. 42, No. 2, 2005, pp. 299–319. doi:10.2514/1.5269.

[3]   Gursul, I., "Recent Developments in Delta Wing Aerodynamics," The Aeronautical Journal, Vol. 108, No. 1087, 2004, pp. 437–452. doi:10.1017/S0001924000000269.

[4]   Gursul, I., Gordnier, R., and Visbal, M., "Unsteady Aerodynamics of Non-Slender Delta Wings," Progress in Aerospace Sciences, Vol. 41, No. 7, 2005, pp. 515–557. doi:10.1016/j.paerosci.2005.09.002.

[5] Wentz, W. H., and Kohlman, D. L., "Vortex Breakdown on Slender Sharp-Edged Wings," Journal of Aircraft, Vol. 8, No. 3, 1971, pp. 156–161. doi:10.2514/3.44247.

[6] Hummel, D., John, H., and Staudacher, W., "Aerodynamic Characteristics of Wing-Body-Combinations at High Angles of Attack," 14th Congress of the International Council of the Aeronautical Sciences, ICAS Paper 2.7.1, September 1984.

[7] Verhaagen, N. G., and Jobe, C. E., "Wind-Tunnel Study on a 65-deg Delta Wing at Sideslip," Journal of Aircraft, Vol. 40, No. 2, 2003, pp. 290–296. doi:10.2514/2.3092.

[8] Johnson, J. L., Grafton, S. B., and Yip, L. P., "Exploratory Investigation of the Effects of Vortex Bursting on the High Angle-of-Attack Lateral-Directional Stability Characteristics of Highly-Swept Wings," AIAA Paper 1980-0463, 1980. doi:110.2514/6.1980-463.

[9] Chambers, J. R., and Anglin, E. L., "Analysis of Lateral-Directional Stability Characteristics of a Twin-Jet Fighter Airplane at High Angles of Attack," NASA-TN-D-5361, August 1969.

[10] Greer, H. D., "Summary of Directional Divergence Characteristics of Several High-Performance Aircraft Configurations," NASA-TN-D-6993, November 1972.

[11] John, H., and Kraus, W., "High Angle of Attack Characteristics of Different Fighter Configurations," Specialists' Meeting on "High Angle of Attack Aerodynamics", AGARD Conference Proceedings, Vol. CP-247, AGARD, 1978, pp. 2.1–2.15.

[12] Staudacher, W., Laschka, B., Poisson-Quinton, P., and Ledy, J. P., "Aerodynamic Characteristics of a Fighter-Type Configuration During and Beyond Stall," Specialists' Meeting on "High Angle of Attack Aerodynamics", AGARD Conference Proceedings, Vol. CP-247, AGARD, 1978, pp. 8.1–8.15.

[13] Hummel, D., and Brümmer, A., "Aerodynamics of a Slender Wing with Vertical Fins at Low Speed," 19th Congress of the International Council of the Aeronautical Sciences, ICAS Paper 4.3.4, September 1994.

[14] Ward, D. T., and Erb, R. E., "Use of Hinged Strakes for Lateral Control at High Angles of Attack," AIAA Paper 1986-2278, 1986. doi:10.2514/6.1986-2278.

[15] Brandon, J. M., Murri, D. G., and Nguyen, L. T., "Experimental Study of Effects of Forebody Geometry on High Angle of Attack Static and Dynamic Stability and Control," 15th Congress of the International Council of the Aeronautical Sciences, ICAS Paper 5.4.1, September 1986.

[16] Rao, D. M., Murri, D. G., and Moskovitz, A., "Forebody Vortex Management for Yaw Control at High Angles of Attack," Journal of Aircraft, Vol. 24, No. 4, 1987, pp. 248–254. doi:10.2514/3.45433.

[17] Tristrant, D., Renier, O., and Farcy, D., "Flow Analysis and Control Surface Evaluation at High Angles of Attack for Enhanced Manoeuvrability," 20th Congress of the International Council of the Aeronautical Sciences, ICAS Paper 3.1.2, September 1996.

[18] Hitzel, S. M., and Osterhuber, R., "Enhanced Maneuverability of a Delta-Canard Combat Aircraft by Vortex Flow Control," Journal of Aircraft, Vol. 55, No. 3, 2017, pp. 1090–1102. doi:10.2514/1.C034473.

[19] Raffel, M., Willert, C. E., Wereley, S. T., and Kompenhans, J., Particle Image Velocimetry - A Practical Guide, 2nd ed., Springer Verlag, ISBN 978-3-540-72307-3, 2007.

[20] Buzica, A., Breitsamter, C., "Turbulent and Transitional Flow Around the AVT-183 Diamond Wing," Aerospace Science and Technology, Vol. 92, 2019, pp. 520-535, doi.org/10.1016/j.ast.2019.06.025.

[21] Pfnür, S., Breitsamter, C., "Leading-Edge Vortex Interactions at a Generic Multiple Swept Wing Aircraft Configuration," Journal of Aircraft, Article in Advance, 2019, pp. 1–15. doi: /10.2514/1.C035491

[22] Johnson, J. L., "Investigation of the Low-Speed Stability and Control Characteristics of a 1/10-Scale Model of the Douglas XF4D-1 Airplane in the Langley Free-Flight Tunnel," NACA-RM-SL51J22, January 1951.